CSIRO PUBLISHING

RESEARCH FRONT

Environ. Chem. **2014**, *11*, 566–578
http://dx.doi.org/10.1071/EN14011

Research Paper

Solid-phase characterisation of an effective household sand filter for As, Fe and Mn removal from groundwater in Vietnam

Andreas Voegelin,[A,E] *Ralf Kaegi*,[A] *Michael Berg*,[A] *Katja Sonja Nitzsche*,[B] *Andreas Kappler*,[B] *Vi Mai Lan*,[C] *Pham Thi Kim Trang*,[C] *Jörg Göttlicher*[D] *and Ralph Steininger*[D]

[A]Eawag, Swiss Federal Institute of Aquatic Science and Technology, CH-8600 Dübendorf, Switzerland.
[B]University of Tübingen, Department of Geosciences, Geomicrobiology Group, D-72074 Tübingen, Germany.
[C]Center for Environmental Technology and Sustainable Development (CETASD), VNU University of Science, 10000 Hanoi, Vietnam.
[D]Karlsruhe Institute of Technology, ANKA Synchrotron Radiation Facility, D-76344 Eggenstein-Leopoldshafen, Germany.
[E]Corresponding author. Email: andreas.voegelin@eawag.ch

Environmental context. Household sand filters are widely used in Vietnam to remove As, Fe and Mn from groundwater used as drinking water. From the solid-phase characterisation of a sand filter that has been used for 8 years, we conclude that As and Fe are retained by a combination of fast sorption reactions, surface-catalysed Fe oxidation and mediated As co-oxidation and that microbial processes are probably involved in effective Mn retention. This study contributes to a better mechanistic understanding of filter functioning as a basis for further improvements in filter design and operation.

Abstract. Household sand filters are widely used in Vietnam to remove As, Fe and Mn from anoxic groundwater used as a drinking water resource. To expand the mechanistic knowledge of the filter functioning, we investigated the bulk and micrometre-scale distribution of Fe, As, P and Mn and the speciation of Fe, Mn and As in a sand filter after 8 years of operation using bulk and micro-focussed X-ray fluorescence spectrometry (XRF) and X-ray absorption spectroscopy (XAS) and scanning electron microscopy coupled with energy dispersive X-ray detection (SEM-EDX). Effective oxygenation of the anoxic groundwater enables the oxidative removal of Fe, As and Mn in the filter sand. Our results show that Fe is retained in the filter as a 2-line ferrihydrite-like Fe^{III}-precipitate that coats sand grains, and that As accumulates dominantly as pentavalent arsenate. The very close spatial correlation of accumulated As and P with Fe throughout the filter sand and down to the micrometre-scale and the effective Fe, P and As retention at an estimated average water residence time of only 30 min suggest that their uptake is governed by a combination of fast sorption reactions, surface-catalysed Fe^{II} oxidation and mediated As^{III} co-oxidation. In contrast, Mn is retained in separate $Mn^{IV/III}$-(oxyhydr)oxide coatings and concretions, probably as a result of coupled surface-catalysed and microbial Mn^{II} oxidation. Silicate sorbed to the ferrihydrite-like Fe^{III}-coatings inhibits their crystallisation and associated remobilisation of P and As. The periodic drainage and aeration of the filter favours the oxidation of any residual Fe^{II} and As^{III} and the formation of dense Fe precipitates and may thereby contribute to effective filter operation over several years.

Additional keywords: drinking water, phosphate.

Received 13 January 2014, accepted 5 May 2014, published online 30 July 2014

Introduction

The use of As-rich anoxic groundwaters as a drinking water resource poses a serious threat to the health of some 100 million people in South and South-east Asian countries.[1–3] These groundwaters may contain As at levels exceeding the World Health Organization (WHO) drinking water guideline of 10 μg L^{-1} by 10 to 100 times, causing skin diseases, heart, liver and kidney problems, diabetes and various kinds of cancer.[2] At the same time, these waters often contain high levels of Fe^{II} and Mn^{II} due to reductive mobilisation with As^{III} in the subsurface.[1,3–6] Both Fe and Mn are nuisance chemicals that affect the taste and aesthetics of drinking water. In Vietnam, household sand filters were found to provide an effective means to remove As, Fe and Mn from groundwater, with (weight-based) Fe/As ratios >250 typically ensuring As removal to levels below 10 μg L^{-1}.[7,8]

Many of the individual geochemical and microbial processes contributing to the removal of Fe, As and Mn from aerated groundwater in sand filters are well documented. Iron removal is driven by the oxidation of dissolved Fe^{II} to poorly soluble Fe^{III} and its precipitation in the filter matrix.[9] At near-neutral pH, Fe^{II} oxidation includes the homogeneous oxidation of dissolved Fe^{II} by O_2, catalytic oxidation of surface-bound Fe^{II} and, under microaerophilic conditions, microbial Fe^{II} oxidation.[9] Depending on chemical conditions, the structure of the formed Fe^{III} precipitates ranges from poorly crystalline lepidocrocite over ferrihydrite-type hydrous ferric oxide to amorphous Fe^{III}-phosphate.[10–13] The abiotic oxidation of dissolved Fe^{II} also mediates the co-oxidation of arsenite (As^{III}) to more strongly sorbing arsenate (As^{V}).[14] In addition, microorganisms may oxidise As^{III} through respiration or detoxification pathways.[15] Both As^{III} and As^{V} compete with phosphate and silicate for co-precipitation with the forming Fe^{III} precipitates.[16,17] At near-neutral pH, the homogeneous oxidation of dissolved Mn^{II} by O_2 does not proceed at a significant rate and removal of Mn by oxidation to poorly soluble Mn^{IV} is driven by surface-catalysed and microbial oxidation processes.[18–21] $Mn^{III/IV}$ oxides accumulated in sand filters may also contribute to improved Fe and As removal by acting as an effective oxidant for both Fe^{II} and As^{III}.[22–24]

Although much is known about the individual processes contributing to sand filter performance, the importance and interplay of various (bio)geochemical reaction pathways is still not fully understood and expected to depend on local conditions. The aim of the present study therefore was to shed light on the functioning of effective household sand filters for As removal by investigating the spatial distribution and speciation of Fe, As and Mn in a sand filter after use for ~8 years in a rural household in Vietnam. Specifically, we (i) determined the amounts of As, P, Fe and Mn accumulated in the filter matrix by X-ray fluorescence spectrometry (XRF), (ii) characterised the speciation of accumulated As, Fe and Mn using X-ray absorption spectroscopy (XAS) and (iii) analysed element distributions at the millimetre- to micrometre-scale using micro-focussed (μ-) XRF and XAS and scanning electron microscopy coupled with energy dispersive X-ray detection (SEM-EDX).

Materials and methods

Sand filter characterisation

The sand-filter studied in this work (Fig. 1) was located in the village Van Phuc in the rural outskirts of Hanoi, Vietnam. The sand used in the filter had been collected from the nearby Red River and exhibited a broad size distribution (~25 % fine gravel, ~75 % coarse to very fine sand). The sand was contained in a rectangular concrete tank with a surface area of 83×57 cm^2 and a depth of 52 cm. The sand layer was 43 cm high, resulting in a sand volume of ~0.20 m^3. Based on a bulk density of 1470 ± 110 kg m^3 and a porosity of 35 ± 5 % (mean and standard deviation; derived from volume and weight of four sand samples in dry and water saturated state), the filter was calculated to contain ~300 kg of sand with a pore volume of ~71 L (and ~42 L of water storage volume on top of the sand surface). According to the owner, the filter was typically used twice a day with intermittent filter drainage. Groundwater from the owner's shallow tubewell was pumped through a hose onto the sand surface on the left side of the filter at a rate of ~12 L min^{-1}. The water rapidly infiltrates through the sand and drains through two outlets at the bottom of the filter (effluent water) into a storage tank (Fig. 1) at a rate of 2.6 ± 0.1 L min^{-1}. During pumping, the water level above the sand surface rose until the water overflows after ~10 min. At this point, the pump was switched off and the filter was allowed to drain. Two operation cycles per day thus corresponded to the treatment of ~240 L of groundwater per day. Combined with the estimated pore volume of ~71 L, the effluent flow rate of 2.6 L min^{-1} translates into a residence time of the water in the filter sand of ~30 min under plug flow conditions. However, incomplete drainage of water between consecutive filtration cycles may have substantially enhanced the residence time of a part of the water, whereas another fraction may have passed the filter considerably faster due to rapid infiltration and preferential flow. At the time of the collection of sand samples (April 2010), the filter had been in use for ~8 years and was still operated with the originally added sand, except for the annual replacement of the topmost 2–3 cm of sand with fresh sand.

Water sampling and analysis

Raw groundwater (influent) delivered to the sand filter was sampled in 2009 (duplicates), 2010 (triplicates) and 2012 (19 samples), treated water draining out of the filter (effluent) was sampled in 2010 (triplicates). The water samples were passed through 0.22-μm membrane filters and acidified on site for the analysis of total element concentrations using inductively coupled plasma mass spectrometry (ICP-MS, Agilent 7500ce, Agilent Technologies, Santa Clara, CA, USA).

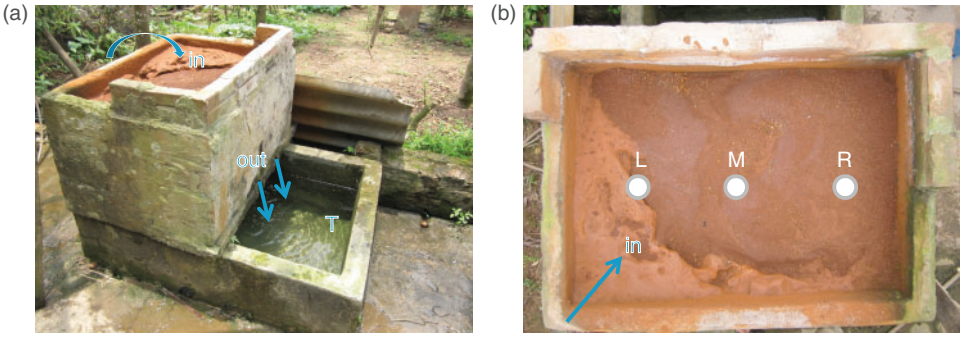

Fig. 1. (a) Side view and (b) top view of studied sand filter. Water is pumped onto the sand on the left side of the filter ('in'). Through two outlets ('out'), the water trickles into the storage tank ('T'). Approximately 10 cm-long sand cores of 2.5-cm diameter were collected on the left ('L'), in the middle ('M') and on the right ('R') side of the filter (filled grey circles) at three depths (0–10 cm, 15–25 cm, 30–40 cm). In panel (b), the cemented sand surface in the left part of the filter can be seen.

Sand sampling

As indicated in Fig. 1b, undisturbed sand cores of 2.5-cm diameter and 9–10-cm length were collected in 50-mL polyethylene tubes on the left, in the centre and on the right side of the filter at depths of 0–10 (top), 15–25 (middle) and 30–40 cm (bottom). The cemented sand surface on the left side of the filter where the water is entering was sampled separately. In the laboratory, the cores were frozen, cut into an upper and a lower part and freeze-dried. Most material from the upper half of each core was powdered using a mixer mill with ZrO_2 jars (MM400, Retsch GmbH, Haan, Germany) for analysis by XRF and XAS as well as for acid digestion and acid-oxalate extraction. From the three vertical samples from the middle of the filter, fine material and coatings on quartz grains were gently separated from sand grains in an agate mortar for separate analysis by Fe K-edge XAS. The lower part of each core was embedded in two-component epoxy-resin and prepared as 30 μm-thick polished thin-section on As-free glass slides (Thomas Beckmann, Schwülper-Lagesbüttel, Germany) for analysis by light microscopy, μ-XRF, μ-XAS and SEM-EDX.

Total and oxalate-extractable element contents and bulk mineralogy of filter sand

Total element contents were determined using energy-dispersive X-ray fluorescence spectrometry (XEPOS+, SPECTRO Analytical Instruments GmbH, Kleve, Germany). For XRF analysis, the powdered samples were further ground and homogenised using a mixer mill with tungsten carbide jars, mixed with wax and pressed into 32-mm pellets. Quantification was based on a build-in calibration for geological samples. The analysis of three reference materials and three synthetic P-containing Fe-coated quartz samples (mixtures of quartz sand, goethite and Fe-phosphate) (Table S1) indicated that instrument-derived As, Fe and Mn were typically within ~10 % of the reference values. Results for the synthetic Fe-coated quartz samples, however, suggested that effective total P concentrations may have been ~25 % lower than derived from XRF analysis (Table S1). The overestimation of total P by XRF may have been due to insufficient sample homogeneity related to the specific sample structure (Fe and P on the surface of quartz grains) and possibly poor deconvolution of the P Kα fluorescence line next to the ~200–800 times more intense Si Kα line. For the determination of acid-extractable Fe, Mn, As, P and Ca, the sand samples were extracted with HNO_3 and H_2O_2 in a microwave oven (50 mg of powdered material; 1.5 mL of 65 % HNO_3 + 0.1 mM 30 % H_2O_2; 180 °C for 10 min; ultraCLAVE 4, MLS GmbH, Leutkirch, Germany) and the extract was analysed by ICP-MS. Acid-extractable contents of Fe, Mn and As (Table S2) were in general agreement with XRF-derived total contents (Table S2). Acid-extractable P contents, however indicated an overestimation of total P by XRF analysis (of the same magnitude as indicated by XRF results for synthetic Fe-coated quartz samples; Table S1) or incomplete P extraction or recovery in the microwave-assisted acid digestion (Table S2).

Acid oxalate-extractable contents of Fe, As, P and Si were determined by extracting 50 mg of the powdered sand samples with 40 mL of 0.2 M NH_4-oxalate solution at pH 2.5 (extraction for 2 h at 29 °C in the dark; analyses by ICP-MS).

To characterise the bulk mineralogy of the sand, selected samples were analysed by X-ray diffraction (XRD) using Co Kα radiation (X'Pert Powder diffractometer with XCelerator detector, PANalytical, Almelo, the Netherlands).

Synchrotron-based spectroscopic analyses

On two thin-sections of filter sand from ~5–10-cm depth (middle, right), three areas of ~10 mm^2 each were analysed by μ-XRF and μ-XAS. These analyses were performed at the SUL-X beamline at ANKA (Angströmquelle Karlsruhe, Eggenstein-Leopoldshafen, Germany) under vacuum at room temperature. Beam energy was monochromatised using a Si(111) fixed-exit double crystal monochromator. Focussing of the X-ray beam was achieved with a Kirkpatrick Baez mirror system. μ-XRF measurements were performed with a ~50 or 60-μm beam and step sizes of 35 or 40 μm at X-ray energies of 12.5 keV (to collect X-ray fluorescence emission of Fe and As) and 6.6 or 7 keV (below Fe K-edge for more sensitive detection of Mn, Ca, K, and Si). The incident photon flux was registered with an ionisation chamber, and the fluorescence signal was recorded using a seven-element Si(Li) solid state detector (Gresham (now SGX Sensortech), High Wycombe, UK). On selected points of interest, μ-XAS measurements were performed at the K-edges of As, Fe and Mn. Beam energies were calibrated by setting the first inflection point of the first-derivative of the absorption edge of Au (for As analyses), Fe and Mn metal foils to 11919, 7112 and 6539 eV. Using a collimated beam (~1-mm diameter), bulk XAS data were recorded on powdered samples pressed into 13-mm pellets either in transmission (Fe) or fluorescence mode (As, Mn) at room temperature. Additional Fe K-edge XAS spectra of powdered bulk samples and isolated fine materials were recorded at the Swiss Norwegian Beamline (SNBL) at the European Synchrotron radiation facility (ESRF, Grenoble, France) in transmission mode at room temperature using a Si(111) double crystal monochromator for energy selection (detuned to 70 % of the maximum intensity for rejection of higher harmonics) and ion chambers for the measurement of incident and transmitted photon flux.

For the extraction of the normalised X-ray absorption near edge structure (XANES) and the X-ray absorption fine structure (EXAFS) spectra and for data evaluation by linear combination fit (LCF) analysis the software code *Athena* was used.[25] LCF analysis of the Fe K-edge EXAFS and Mn K-edge XANES spectra was based on collections of Fe and Mn reference spectra from which the most suitable spectra were selected based on preliminary fits. The selected spectra were included in all final fits with individual fractions constrained to values between 0 and 1.

SEM-EDX analyses

Elemental distribution maps were recorded with a scanning electron microscope (NOVA NanoSEM230, FEI, Hillsboro, OR, USA) operated at an acceleration voltage of 15 kV and equipped with an energy dispersive X-ray analysis system (X-MAX 80, Oxford Instruments, Oxford, UK). Elemental distribution maps of large areas were obtained by an automated recording of EDX counts of 270 individual images corresponding to an area of ~10 mm^2. The pixel resolution of the backscattered electron (BSE) image was 0.2 μm and the elemental distribution maps were recorded at a pixel resolution of 0.4 μm later binned to 0.8 μm (2 × 2 pixels). Selected BSE and elemental distribution maps were exported using the *INCA* software (The Microanalysis Suite, V.18d, Oxford Instruments) and stitched together with *Fiji*.[26,27]

On selected areas (Mn-rich coatings), individual elemental distribution maps (single images) were recorded over several hours to increase the signal-to-noise ratio. For these

measurements, the drift correction method available in the *INCA* software was activated. The pixel resolution of BSE images was 0.07 μm and the pixel resolution of the elemental distribution maps was 0.14 μm later binned to 0.28 μm (2 × 2 pixels).

Results

Water chemistry

Data on the chemistry of the raw groundwater and the treated effluent water are given in Table 1. For the influent, mean element concentrations from samples collected in 2009, 2010 and 2012 are reported (results for individual years in Table S3). The raw groundwater contained elevated concentrations of As (114 ± 17 μg L^{-1}), Fe (16.0 ± 0.2 mg L^{-1}) and Mn (1.27 ± 0.07 mg L^{-1}). These concentrations were well within the range reported for As-affected groundwater in the Red River delta[3,7,28] and the standard deviations (from three sampling dates over 4 years) indicated that the composition of the shallow groundwater was fairly stable. The effluent concentration of As (6 ± 1 μg L^{-1}) recorded in 2010 was below the WHO drinking water guideline of 10 μg L^{-1} and indicated that As was effectively retained in the filter sand (~94 ± 2 % removal), as confirmed by extensive tests on filter performance conducted in 2012.[29] Comparison of the influent and effluent concentrations showed that also Fe, P and Mn were effectively retained. The effluent concentrations of Si, Ca and Mg, on the other hand, showed that Si, Ca and Mg retention was limited, but were too similar to the influent concentrations to precisely quantify the minor fractions (<10 %) retained. Results obtained in 2012[29] showed that the anoxic groundwater and the filter effluent exhibited near-neutral pH (Table 1) and demonstrated that dissolved Fe and As in the raw groundwater were mainly present in their reduced forms Fe^{II} and As^{III}. The O_2 concentration in the effluent of ~5.4 mg L^{-1} O_2 showed that the anoxic groundwater became effectively oxygenated, which is essential for effective oxidative removal of Fe, As and Mn.

Mineralogy and composition of bulk filter material

The qualitative evaluation of XRD patterns collected on three sand samples (Fig. S1) indicated that the filter sand consisted mainly of quartz with minor fractions of feldspar, calcite and primary phyllosilicates (chlorite and mica), in line with mean contents (standard deviation in parentheses; $n = 9$) of 36 % (2 %) Si, 5.0 % (0.5 %) Al, 2.0 % (0.2 %) K, and 1.4 % (0.5 %) Ca determined by XRF spectrometry on the nine bulk samples. Cementation of the sand surface on the left side of the filter was probably due to enhanced $CaCO_3$ precipitation, considering that the cemented sand crust consisted of 11 % acid-extractable Ca.

The total contents of As, P, Mn and Fe determined by XRF spectrometry are listed in Table 2 and shown in Fig. 2. The results reflect the substantial accumulation of As in the filter, with solid-phase As concentrations decreasing from the top left to the bottom of the filter (Fig. 2a). The cemented sand surface on the left side of the filter may have hampered local water infiltration resulting in a lower As content in the underlying sand. Total As and P very closely correlated with Fe (Fig. 2b, d), suggesting concomitant retention in the filter matrix at the macroscopic scale. A less close correlation was observed between Mn and Fe (Fig. 2c).

Molar oxyanion/Fe ratios derived from oxalate-extractable Fe, P, Si and As contents revealed only minor variations between the ten samples (Table S4; Si/Fe = 0.21 ± 0.03, P/Fe = 0.063 ± 0.005, As/Fe = 0.0062 ± 0.0005; $n = 10$), pointing to the accumulation of P and As with Fe in a similar type of phase throughout the filter matrix. The molar Si/Fe ratio in the oxalate extract (0.21; Table S4) in comparison to the ratio in the influent groundwater (2.1, Table 1) indicated that ~10 % of the Si contained in the groundwater were retained in the filter sand.

Element distribution in thin-sections by synchrotron-based μ-XRF and SEM-EDX

To explore spatial element correlations at smaller scales, two thin-sections prepared from material from the top sand layer (middle and right) were investigated by light microscopy, synchrotron-based μ-XRF mapping, and SEM-EDX analysis (Figs 3, 4). The elemental distribution maps of Fe, K and Si in Fig. 3b indicated the presence of quartz (Si only, green), K-feldspar (K and Si; orange) and chlorite (Fe-rich, blue; Si not visible due to intensity scaling) grains. The maps for Fe and As (Fig. 3c) indicated that most sand grains were covered with As-containing Fe-rich coatings, whereas Mn was concentrated in concretions and Mn-rich coatings at fewer locations (see also maps in the Supplementary material collected on other areas). In the plot of As *v.* Fe counts (Fig. 3d), points with relatively high and constant As/Fe ratios (Fig. 3e, pink dots) correspond to As-containing Fe coatings which were also readily visible as brown coatings in the light microscope image (Fig. 3a). These points can be clearly discerned from pixels with low As/Fe ratios that represent Fe-rich mineral grains. Points with intermediate As/Fe ratios reflect pixels with contributions from both Fe coatings and mineral grains. The colour in Fig. 3e, which is indicative for the As/Fe ratio in accumulated Fe coatings, did not differ in Mn-rich

Table 1. Characterisation of sand filter influent (raw groundwater) and effluent (treated water)

pH and dissolved O_2 in influent and effluent were measured on-site in 2012 using flow cell electrodes (pH: $n = 4$, s.d. = 0.0; $O_{2(aq)}$: $n = 6$).[29] Influent concentrations of As, P, Fe, Mn, Ca and Mg correspond to arithmetic mean (and standard deviation) from groundwater samples collected in 2009, 2010 and 2012, the influent concentration of Si corresponds to the mean (and standard deviation) of triplicate samples collected in 2010. All effluent concentrations correspond to the mean (and standard deviation) of triplicate samples collected in 2010. Detailed results for 2009, 2010, and 2012 are given in the supplementary material (Table S3). Influent data for As/Fe, P/Fe and Mn/Fe are molar element ratios. For As/Fe, P/Fe and Mn/Fe, the mean (and standard deviation) of ratios in samples collected in 2009, 2010 and 2012 are given, for Si/Fe the ratio was determined in 2010. For results from individual years see Table S3

Sample	pH	$O_{2(aq)}$ (mg L^{-1})	As (μg L^{-1})	P (μg L^{-1})	Si (mg L^{-1})	Fe (mg L^{-1})	Mn (mg L^{-1})	Ca (mg L^{-1})	Mg (mg L^{-1})
Influent	6.9	<0.1	114 (±17)	560 (±130)	16.6 (±0.3)	16 (±0.2)	1.27 (±0.08)	171 (±5)	36.9 (±1.2)
Effluent	7.1	5.4 (±0.4)	6.2 (±1.1)	<5	15.6 (±0.2)	<0.1	<0.01	157 (±13)	38.8 (±0.4)
			As/Fe	P/Fe	Si/Fe		Mn/Fe		
Influent			0.0053 (±0.0008)	0.063 (±0.015)	2.1 (–)		0.08 (±0.005)		

Table 2. Total element contents in bulk samples determined by X-ray fluorescence spectroscopy (XRF)

Depth interval of bulk samples used for XRF analysis. Average data are arithmetic mean of contents in nine bulk samples measured by XRF (without crust sample). Background contents data are of P, Mn and Fe in sand estimated from linear regressions of P, Mn or Fe *v*. As for an assumed As background content of 0 mmol kg^{-1} (Fig. S2). Accumulated contents data are arithmetic mean from XRF analyses minus background contents. X/Fe_{acc} data are molar As/Fe, P/Fe, and Mn/Fe ratios calculated from estimated accumulated amounts in each sample; values in parentheses indicate standard deviation ($n = 9$)

Location	Depth (cm)	As (mmol kg^{-1})	P (mmol kg^{-1})	Mn (mmol kg^{-1})	Fe (mmol kg^{-1})
Left (L)	Crust[A]	7.0[A]	86.3[A]	57.9[A]	1542[A]
	0–5	3.84	57.0	45.4	958
	15–20	0.37	15.6	13.6	278
	30–35	0.60	15.5	23.2	289
Middle (M)	0–5	2.92	45.4	37.3	749
	15–20	2.02	33.2	33.0	555
	30–35	1.42	26.4	25.1	441
Right (R)	0–5	3.16	46.2	40.8	799
	15–20	1.96	33.5	27.2	559
	30–35	2.15	31.6	26.9	584
Average		2.05	33.8	30.3	579
Background		0	9.2	13.5	174
Accumulated		2.05	24.7	16.8	405
X/Fe_{acc}		0.0050 (±0.0006)	0.061 (±0.004)	0.041 (±0.021)	

[A]Cemented sand crust formed on left side of filter sand analysed by acid extraction. Amounts correspond to respective molar As/Fe, P/Fe and Mn/Fe ratios of 0.045, 0.056 and 0.038.

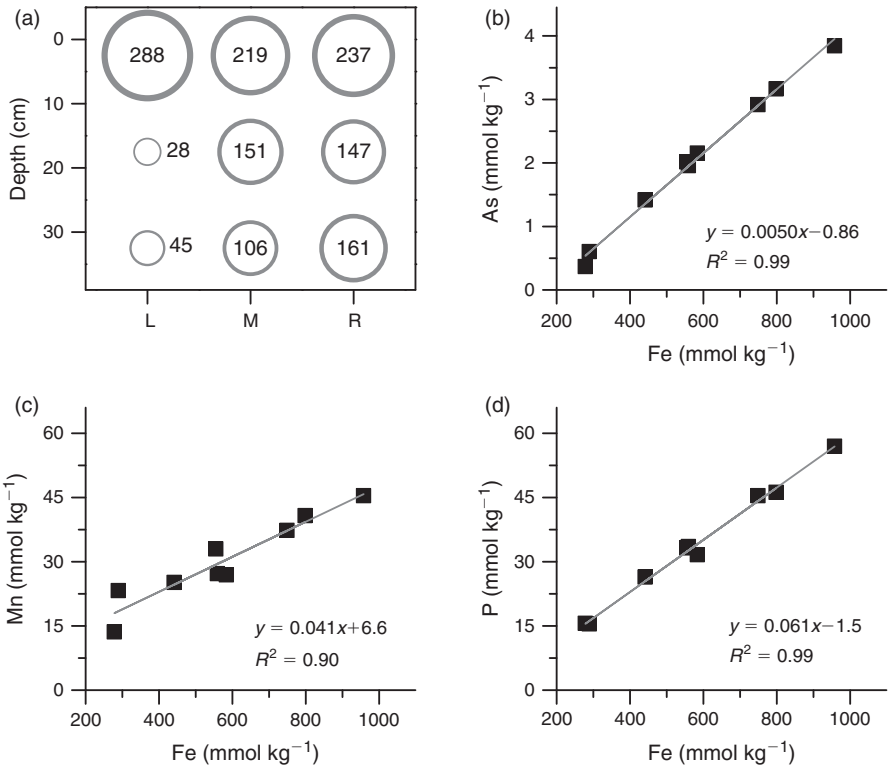

Fig. 2. (a) Total contents of As in nine sand samples collected in a vertical plane through the filter (left (L), middle (M) and right (R) side of filter; at depths of 0–5, 15–20 and 30–35 cm in the sand layer). Bubble area scales with square root of As content, numbers indicate As concentration (mg kg^{-1}). (b–d) Total contents of As, Mn and P as a function of total Fe (squares), linear regressions (lines) and regression parameters ($n = 9$). Data are listed in Table 2.

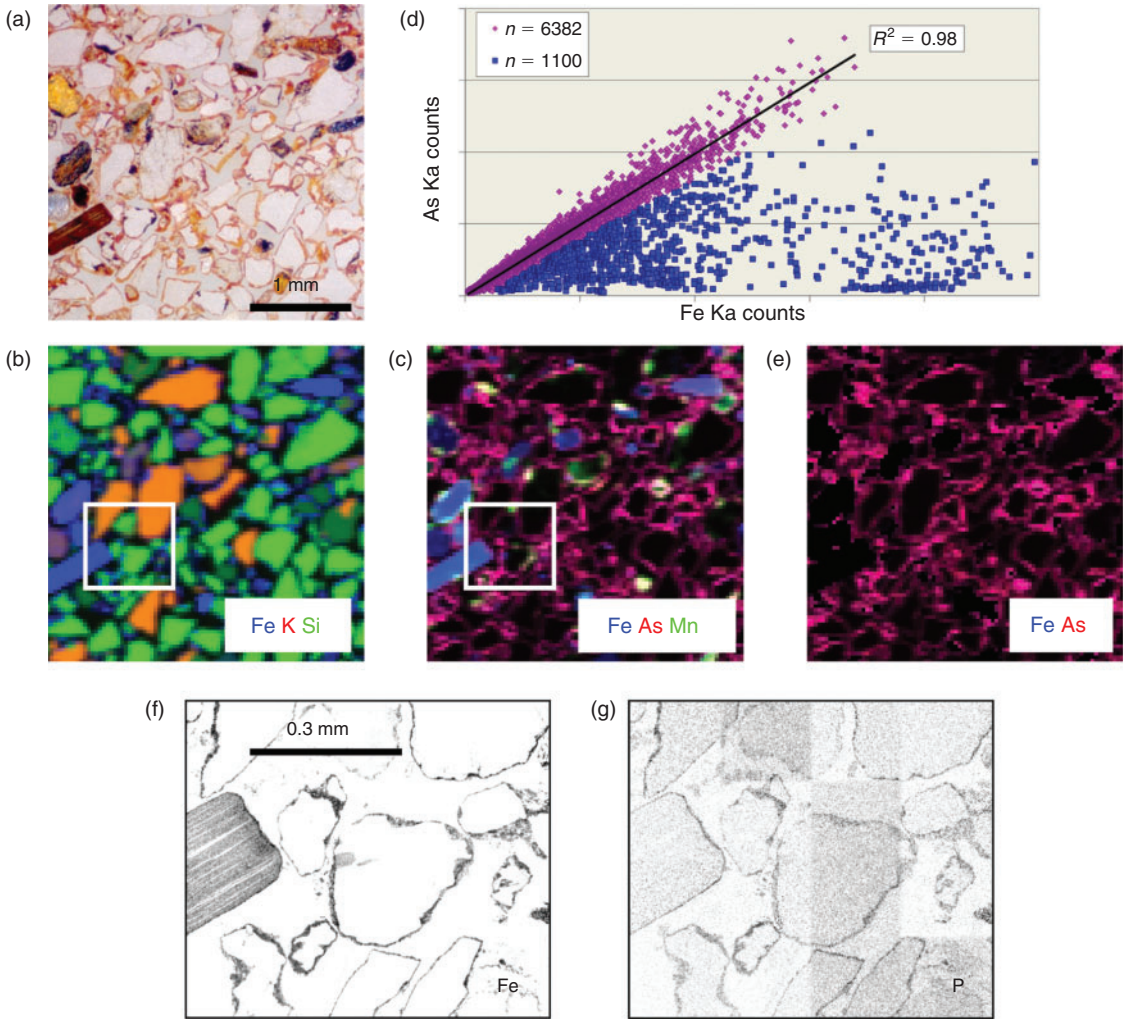

Fig. 3. (a) Light microscope image of thin-section from sand from top-right sample and (b, c) corresponding μ-X-ray fluorescence elemental maps for K–Si–Fe and As–Mn–Fe (area 3.2 × 3.2 mm^2; step size 35 μm, beam size ~50 μm; As and Fe maps recorded at 12.5 keV, Mn, K, and Si at 6.6 keV). (d) Correlation of As Kα *v*. Fe Kα counts for map shown in panel (c) and (e) filtered elemental distribution map for pink-coloured points in panel (d). (f, g) Scanning electron microscopy elemental distribution maps (inverted grayscale) for Fe and P in area marked by white squares in panels (b) and (c). In panels (b) and (c), white level corresponds to zero counts and black level was defined as the count level corresponding to 85 % (Fe) or 95 % (Mn, As) of the cumulative counts of the mapped area.

zones (coatings, concretions). This indicated that local Mn accumulations did not affect As–Fe interactions in their vicinity. The analysis of a sub-area by SEM-EDX showed that the Fe coatings were only a few tens of micrometres thick (Fig. 3f). Whereas As was not detectable by EDX, the EDX-derived P map revealed the same close spatial correlation with Fe (Fig. 3f, g) as observed for As and Fe by μ-XRF (Fig. 3e). Mn was not detectable by EDX in pure Fe coatings, in line with low Mn/Fe ratios of the order of ~0.01 qualitatively estimated from μ-XRF-derived Mn and Fe intensities.

The black Mn-rich coating around one quartz grain was evaluated in more detail using μ-XRF and SEM-EDX (Fig. 4). The elemental distribution maps derived from μ-XRF measurements confirmed the high Mn-content of black coatings. However, even in black coatings, Mn counts were typically not higher than Fe counts, indicating that the black coatings contained both Mn- and Fe-bearing phases. SEM-EDX analysis of the areas A and B conducted at a higher special resolution (Fig. 4c–f) showed that the Mn- and Fe-rich coatings consisted of an intimate but clearly separate association of pure Mn or Fe precipitates, with thin Fe coatings often covering more extensive Mn precipitates. EDX analysis revealed that P was exclusively associated with the Fe phase which also contained a minor fraction of Mn, whereas the Mn phase did not contain detectable levels of P and Fe (Fig. S5, Supplementary material). In contrast to P, As was below the detection limit of SEM-EDX.

Speciation of Fe, Mn and As by XAS

The speciation of Fe, Mn and As in the filter material was mainly assessed by K-edge XAS on bulk samples. In addition, μ-XAS data for As and Mn were collected on thin-sections. The Fe K-edge EXAFS spectra of bulk samples and fine material (separated from bulk samples by gentle grinding) in comparison to reference spectra used for LCF analysis are shown in Fig. 5. Based on preliminary fits using a reference spectra database including amorphous and crystalline Fe^{III}-(oxyhydr)oxides, magnetite, vivianite, Fe^{II}- and Fe^{III}-containing phyllosilicates, organically complexed Fe^{III} and Fe^{II} and Fe^{III} salts, the following four references were found to account for all spectral

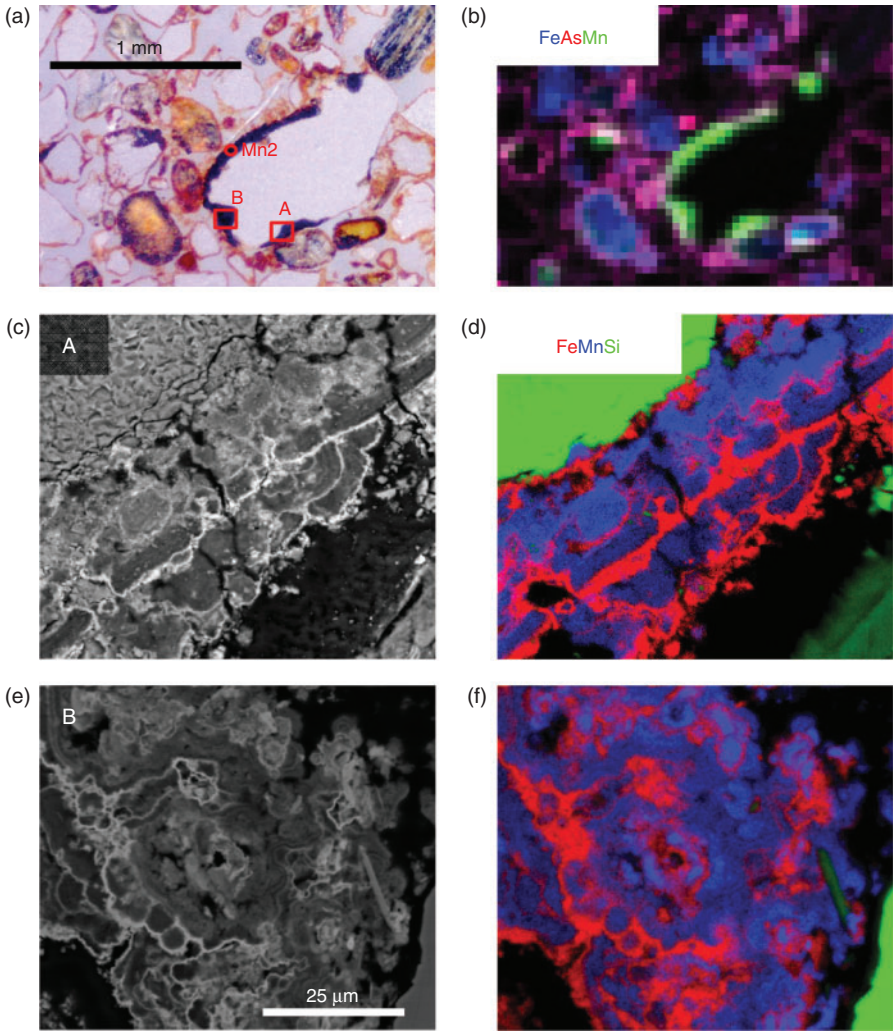

Fig. 4. (a, b) Light microscope image of thin-section from sand from top-middle and corresponding µ-X-ray fluorescence (-XRF) elemental map for Fe–As–Mn. (c, e) Scanning electron microscopy backscattered electron images and (d, f) corresponding tricolour distribution maps (Fe–Mn–Si) in a Mn–Fe coating around a quartz grain (areas A and B marked in panel a). Scale bar in panel (e) applies to panels (c–f). The entire area mapped by µ-XRF is shown in Fig. S4. Label Mn2 in panel (a) indicates point analysed by Mn K-edge X-ray absorption near edge structure (XANES) (Fig. 6).

features in the sample spectra and were included in final LCF analysis: goethite, 2-line ferrihydrite, amorphous Fe^{III}-phosphate and chlorite. Results obtained by LCF analyses based on these reference spectra are listed in Table 3. Considering the total Fe contents and the estimated background Fe content (Table 2), the fraction of accumulated Fe over total Fe in the studied samples ranged from 77 % in the sample from the top to 61 % in the sample from the bottom of the filter. Accordingly, LCF results indicated a minor fraction of Fe contained in chlorite, in line with the observation of chlorite grains in element distribution maps (Fig. 3, 4) and the identification of chlorite by XRD (Fig. S1). The concomitant occurrence of a very small goethite fraction may indicate that in addition to chlorite some goethite was already contained in the fresh sand. In the fine-grained isolates from the same samples, both the goethite and chlorite fractions were reduced (Table 3), indicating that EXAFS results from these samples more closely represented the structure of the accumulated Fe. The respective LCF results showed that the average local Fe coordination of the accumulated Fe^{III} precipitate could be described by a combination of

Table 3. Results from linear combination fitting (LCF) analysis of Fe K-edge X-ray absorption fine structure (EXAFS) spectra

Fits were performed on the k^3-weighted EXAFS spectra over the k-range of 2 to 9.5 $Å^{-1}$ with individual fractions constrained to range between 0 and 100 % but unconstrained sum. Individual fractions normalised to a sum of 100 % and the unnormalised sums are reported. Reference spectra used for LCF analysis included goethite (Goe), 2-line ferrihydrite (Fh), amorphous Fe^{III}-phosphate (FeP) and chlorite (Chl, CCa-2 from the Source Clay Repository, West Lafayette, IN, USA). L Crust data are not shown in Fig. 5.

NSSR (normalised sum of squared residuals) = $\sum(data_i\text{-}fit_i)^2/\sum data_i^2$

	Goe (%)	Fh (%)	FeP (%)	Chl (%)	Sum (%)	NSSR (×1000)
M 0–5	5	51	32	12	106	3.0
M 15–20	6	54	26	15	107	10.5
M 30–35	16	37	31	16	101	9.8
M 0–5 fine	4	55	35	5	108	4.2
M 15–20 fine	0	65	31	4	109	3.2
M 30–35 fine	0	67	30	3	107	2.6
L Crust	2	59	32	7	100	3.0

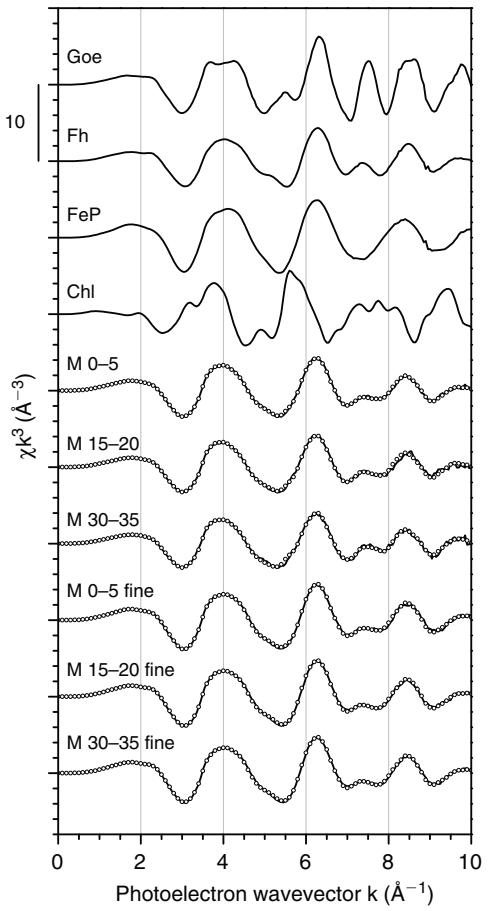

Fig. 5. Fe K-edge X-ray absorption fine structure (EXAFS) spectra of bulk material from three depths from the filter middle, corresponding fine material, reference spectra (solid lines; Goe, goethite; Fh, 2-line ferrihydrite; FeP, amorphous Fe^{III}-phosphate; Chl, chlorite; reference spectra Goe, Fh, FeP from Voegelin et al.[11] and Chl from Frommer et al.[58]), and linear combination fit (LCF) spectra (open symbols). Results from LCF analysis are listed in Table 3.

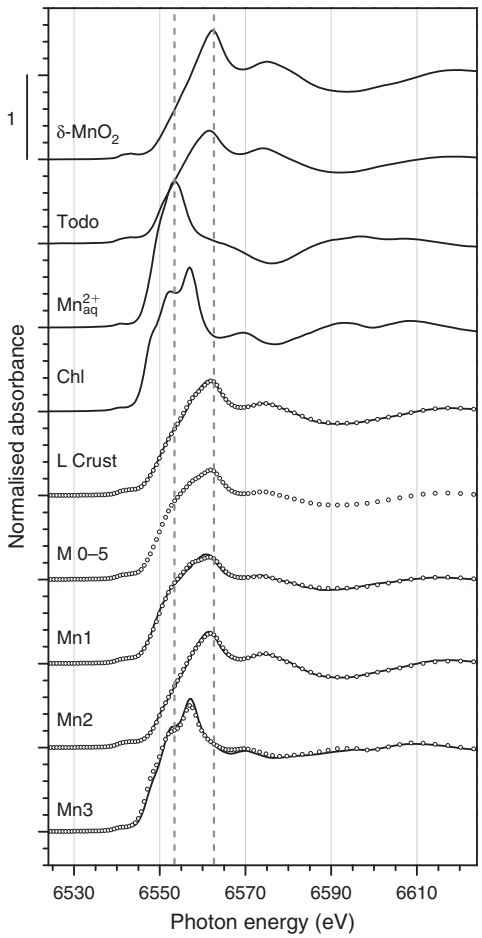

Fig. 6. Mn K-edge XANES spectra (solid lines) of references (δ-MnO_2 and todorokite (Todo) from Webb et al.[59] aqueous Mn^{2+} (Mn^{2+}_{aq}) and Mn in chlorite (Chl) from Frommer et al.[58]), bulk samples (L Crust, M 0–5) and points of interest from two thin-sections (Mn1 (Fig. S3) and Mn2 (Fig. 4a) corresponding to Mn-rich coatings, Mn3 (Fig. S3) to Fe-rich phylloscilicate-type mineral grain). Linear combination fit (LCF) spectra (open symbols) corresponding to LCF results listed in Table 4. Vertical dashed lines at incident photon energies of 6553.4 and 6562.6 eV respectively correspond to the white line maxima of Mn^{II} and Mn^{IV}.

~65 % 2-line ferrihydrite (with edge- and (minor) corner-sharing Fe–Fe linkage) and ~35 % amorphous Fe^{III}-phosphate (accounting for monomeric and oligomeric Fe). A similar result was also obtained for the Fe-rich cemented crust collected on the surface of the sand filter (Table 3), suggesting that Fe retained at the sand surface was not precipitated in markedly different form than Fe removed within the sand matrix. The LCF-based representation of the accumulated Fe^{III} precipitate by a mixture of ~65 % 2-line ferrihydrite and ~35 % amorphous Fe^{III}-phosphate does not imply the formation of two separate Fe^{III} precipitates (for which no evidence was found by μ-XRF, SEM-EDX and oxalate extraction) or a specific content of phosphate or silicate in the precipitate (due to the dominance of the signal of second-shell Fe over P and Si and lacking sensitivity of Fe K-edge EXAFS spectroscopy to differentiate between second-shell P or Si). Instead, the LCF-derived characterisation of the Fe^{III} precipitate shows that Fe accumulates as a ferrihydrite-like phase with a lower degree of edge- and corner-sharing Fe–Fe linkages than in synthetic 2-line ferrihydrite, which can be attributed to co-precipitated Si and P which reduce the extent of Fe^{III} polymerisation.[11,30,31]

The speciation of Mn in the sand filter was assessed by bulk and μ-XANES spectroscopy at the Mn K-edge (Fig. 6). Analysis of the crust formed on the left side of the filter surface and of the top sample from the centre of the filter by LCF showed that Mn was mainly retained as a $Mn^{III/IV}$-(hydr)oxide phase, as also confirmed by LCF results for two μ-XANES spectra collected in Mn-rich zones (Table 4). The analysis of a phyllosilicate-type mineral grain on a thin-section, however, confirmed the presence of $Mn^{III/II}$-bearing primary minerals in the sand. Because $Mn^{III/II}$-bearing minerals influenced the bulk XAS spectra and because beam-induced Mn reduction was observed in some cases using a μ-focussed beam, we did not attempt to further constrain the type of $Mn^{IV/III}$-oxide based on Mn EXAFS spectra.

The analysis of two samples from the top of the filter and of several points of interest on a thin-section by As K-edge XANES spectroscopy confirmed that As was mainly retained as pentavalent As^{V} (Fig. S6, Supplementary material).

Discussion

Estimation of accumulated As, P, Fe and Mn

From linear regressions of total contents of Fe and P *v.* As, the respective background contents in the sand were estimated

Table 4. Results from linear combination fit (LCF) analysis of Mn K-edge XANES spectra

Fits were performed over an energy range of 6534 to 6614 eV with individual fractions constrained to range between 0 and 100 % but unconstrained sum. Individual fractions normalised to a sum of 100 % and the effective fit sums are reported. References used for LCF included δ-MnO_2, todorokite (Todo), 0.2 M aqueous Mn^{2+} (Mn^{2+}_{aq}), and chlorite (Chl, CCa-2 from the Source Clay Repository, West Lafayette, IN, USA). NSSR (normalised sum of squared residuals) = $\sum(data_i\text{-}fit_i)^2/\sum data_i^2$

	δ-MnO_2 (%)	Todo (%)	Mn^{2+}_{aq} (%)	Chl (%)	Sum (%)	NSSR (×1000)
L Crust	45	39	3	12	100	0.1
M 0–5	34	38	17	12	101	0.2
Mn1 (Fig. S3)	18	53	15	14	100	0.4
Mn2 (Fig. 4a)	25	71	0	4	99	0.2
Mn3 (Fig. S3)	0	33	2	64	101	1.9

based on the assumption that the fresh sand was As free (Table 2; Fig. S2b, d). By subtracting these background contents from the total contents, the accumulated contents in each sample (not shown) and the average accumulated contents in the sand filter were estimated (Table 2). The molar ratio of accumulated As/Fe (Table 2) was similar to the molar As/Fe ratio in the influent water (Table 1), indicating the consistency of the results and the approach for estimating accumulated As and Fe fractions in individual bulk samples. The XRF-derived estimates for accumulated Fe and the EXAFS-derived characterisation of accumulated Fe as a ferrihydrite-like precipitate were in line with oxalate-extractable Fe contents (Table S4) which on average accounted for 90 ± 9 % of the estimated accumulated Fe.

For Mn, linear regressions against As (Fig. S2c) and Fe (Fig. 2c) returned lower regression coefficients than regressions between As, Fe and P (Fig. S2b, d; Fig. 2b, d). This indicated that spatially separate accumulation of Mn not only occurred at the micrometre-scale as observed by μ-XRF (Fig. 3) and SEM-EDX (Fig. 4) but probably also affected Mn distribution in the filter at the larger scale. Therefore, estimates for background and accumulated Mn based on total Mn contents and linear regression of Mn *v.* As were considered to be associated with larger uncertainty than estimates for As, Fe and P.

Based on the mean concentrations of accumulated As, P, Fe and Mn in the sand samples (Table 2) and the estimated mass of sand in the filter (300 kg), accumulated amounts were estimated as 0.61 mol (0.46 g) As, 7.4 mol (229 g) P , 122 mol (6.79 kg) Fe and 5.0 mol (276 g) Mn. For comparison, considering that ~108 μg L^{-1} As, 0.56 mg L^{-1} P, 16.0 mg L^{-1} Fe and 1.27 mg L^{-1} Mn were retained in the filter (Table 1), accumulated amounts of 1.01 mol As, 12.7 mol P, 201 mol Fe and 16.2 mol Mn were estimated from information on filter use provided by the owner (treatment of 2 × 120 L per day over 8 years; not considered in this estimate was the annual replacement of the topmost 2–3 cm of sand which may reduce the remaining accumulated amounts by ~5–15 %). For As, P and Fe, estimates of accumulated amounts based on XRF data corresponded to ~60 % of the estimates based on groundwater composition and filter use, whereas for Mn, the XRF-derived estimate accounted for only ~30 % of the estimate derived from filter usage. Although both estimates were based on different types of assumptions, simplifications and analytical uncertainties, their similar magnitude confirmed that the studied filter had indeed been in regular use over several years without replacement of the entire filter sand. Considering that XRF results for Fe and Mn were quite reliable (Table S1) and that Fe and Mn also exhibited fairly stable concentrations in the influent water (Table S3), the much lower percentage of Mn (~30 %) than Fe (~60 %) 'recovered' by the XRF-based estimate relative to the groundwater–operation-based estimate either indicated that localised Mn accumulations were not representatively probed by the nine bulk sand samples or that Mn periodically leached from the filter.

Co-precipitation and removal of Fe and As in aerated groundwater

Regarding the role of influent water composition for effective As removal, an earlier field study on the performance of sand filters in Vietnam showed that Fe/As ratios in the groundwater of >50 (weight-based) normally ensure reduction of effluent As to values <50 μg L^{-1} and Fe/As ratios >250 reduction to <10 μg L^{-1} in sand filters.[7] With an Fe/As ratio of 140, the groundwater treated in the studied filter thus seemed suited for effective As removal.

The simple classification based on an Fe/As ratio mainly accounts for two effects: (i) Mediated co-oxidation of As^{III} to more strongly sorbing As^{V} during Fe^{II} oxidation by O_2[14] and (ii) competition of As^{III} and As^{V} with other oxyanions for uptake by the forming Fe^{III}-precipitates.[16] Because Fe^{II} competes with As^{III} for reaction with reactive intermediates of Fe^{II} oxidation,[14] the fraction of co-oxidised As^{III} in synthetic groundwater was observed to level off at ~50 % for (weight-based) Fe/As ratios exceeding ~20.[16] More effective As removal at even higher Fe/As ratios is therefore mainly due to further reduction of oxyanion competition (more sorption sites). From experiments in synthetic groundwater at pH 7.0, it was found that phosphate and As^{V} sorbed most strongly to fresh Fe^{III} precipitates, with sorption affinities ~100 times higher than for As^{III} and ~1000 times higher than for silicate.[16] Phosphate thus has a much stronger effect on both As^{V} and As^{III} uptake by Fe^{III} precipitates than Si and the relatively low molar P/Fe ratio of ~0.06 of the influent water (Table 1) hence was another key factor enabling effective As removal.[1,7,16] The rather high concentrations of bivalent Mg and especially Ca in the influent (Table 1) contributed to effective As retention by electrostatically enhanced co-sorption with As and other oxyanions[11,32,33] and more specific covalent interactions, especially between Ca and phosphate, which further reduce sorption competition.[11] In addition, the high concentrations of Ca and Mg also have a strong coagulating effect[11,34,35] and prevent the formation of stably dispersed As-bearing Fe^{III} colloids that could otherwise pass the filter matrix.

Thus, based on the composition of the treated groundwater, effective co-precipitation of As and P with Fe in rapidly coagulating Fe^{III} precipitates is expected to occur even in the absence of pre-existing surfaces or microbiological processes, provided that sufficient time for near-complete homogeneous or autocatalytic Fe oxidation is available (half life time of ~20 min for purely homogeneous and of ~15 min for autocatalytic oxidation of 15 mg L^{-1} dissolved Fe^{II} in air-saturated 10 mM bicarbonate electrolyte at pH 7.0[36]). However, noting that a fraction of the treated water may pass the filter along preferential flow paths in less than 30 min, the near-complete removal of Fe, As and Mn suggested that surface-catalysed and possibly microbial processes may also contribute to filter functioning, as will be discussed in more detail in the following sections.

Processes involved in Fe, P and As retention in the filter sand

The O_2 concentration of ~5.4 mg L^{-1} in the filter effluent indicated that the groundwater became effectively oxygenated during treatment. Assuming an O_2 concentration of 8 mg L^{-1} for fully oxygenated water and considering that ~2.7 mg L^{-1} of O_2 is needed for the oxidation of 16.0 mg L^{-1} of Fe^{II} and 1.27 mg L^{-1} of Mn^{II} (to Fe^{III} and Mn^{IV}), the concentration of O_2 in the effluent of ~5.4 mg L^{-1} was quantitatively in line with near-complete groundwater oxygenation (~8 mg L^{-1} O_2) before infiltration into the filter sand and oxidation of the Fe^{II} and Mn^{II} in the stagnant water and the filter sand with negligible further O_2 supply.

The characterisation of Fe by spatially resolved μ-XRF and SEM-EDX (Figs 3, 4) in combination with element speciation by K-edge XAS (Fig. 5, Table 3) indicated that Fe was accumulated as thin coatings of a two-line ferrihydrite-like precipitate on sand grains, in line with earlier studies on the mineralogy of Fe in sand filters used for Fe removal.[37,38] Apart from very minor fractions of goethite which may also have been introduced with the fresh filter sand, no sign of the transformation of the accumulated Fe into a more crystalline Fe-(hydr)oxide phase over a period of up to 8 years was found. This has previously been attributed to co-precipitated silicate which inhibits ferrihydrite crystallisation during precipitate aging[37,39] and thereby also the potential remobilisation of co-precipitated P or As.[40] Indeed, molar ratios of 0.28 ± 0.03 (Si + P + As)/Fe and 0.21 ± 0.03 Si/Fe obtained from the oxalate-extractable contents of Fe, Si, P and As in the sand samples (Table S4) are in line with maximum oxyanion/Fe ratios of ferrihydrite-type precipitates of ~0.25[12] and indicate that silicate saturated the sorption sites that were not occupied by phosphate and arsenate.

Previous work suggested that during Fe^{II} oxidation in initially homogeneous phosphate-containing aqueous solutions, amorphous Fe^{III}-phosphate with a P/Fe ratio of ~0.5–0.8 (depending on Ca) forms first.[10–12] Such a temporal sequence would imply that – under conditions of dissolved Fe oxidation and precipitation along a chromatographic flow path – the precipitate in the uppermost part of the sand filter should have a higher P/Fe ratio than precipitates formed at a greater depth, and that the precipitate type should concomitantly shift from a higher fraction of Fe^{III}-phosphate in the top-most sand layers to ferrihydrite-like at depth. However, based on XRF results for bulk samples (Fig. 2) and Fe EXAFS LCF results for the fine fractions from the sand and the cemented sand crust from the filter surface (Table 3), the P/Fe ratio and structure of the accumulated Fe^{III} precipitate did not vary markedly over depth. This was also supported by the relatively constant molar oxyanion/Fe ratios of the oxalate-extractable Fe^{III} precipitate, including the cemented crust from the top of the sand (Table S4). The homogeneity of the accumulated Fe^{III} precipitate throughout the filter indicates that the uptake of Fe and P may be transport-limited and that transfer to the solid–water interface is followed by rapid sorption of Fe^{II} and phosphate and surface-catalysed Fe^{II} oxidation. Alternatively, at a molar P/Fe ratio of 0.063 in the untreated groundwater (Table 1), initially homogeneous oxidation of only ~10 % of the dissolved Fe^{II} would be sufficient for complete phosphate uptake into colloidal Fe^{III}-phosphate which could then be deposited onto sand grains concomitant with continuing Fe oxidation and precipitation.

Removal of As in the sand filter involves mediated co-oxidation of As^{III} with Fe^{II},[14] followed by effective competition of As^{V} with phosphate for co-precipitation with Fe^{III} and sorption to Fe^{III}-(oxyhydr)oxides.[16] K-edge XANES spectroscopy confirmed that As retained in the filter was dominantly As^{V} (Fig. S6). Over the entire filter sand (Fig. 2) as well as at the micrometre-scale (Fig. 3, 4, S3, S4), As was accumulated together with Fe, in parallel to phosphate. This suggests that As retention was directly coupled to Fe and P removal and probably involved fast sorption and surface-catalysed oxidation reactions on Fe^{III} coatings.

An average accumulated Fe content of 405 mmol kg^{-1} corresponds to ~33 g kg^{-1} ferrihydrite-like Fe coatings (based on an ideal ferrihydrite stoichiometry of $FeO_{1.4}(OH)_{0.2}$ with a molecular weight of 81.7 g mol^{-1}[41]). Considering a packing density of 1.47 kg L^{-1} and a porosity of 35 % of the filter sand, this equals ~139 g L^{-1} of ferrihydrite-like precipitate per pore volume. Even if only 1 % of this precipitate is assumed to be accessible to the passing groundwater, it can be estimated that more than 90 % of the Fe^{II} is adsorbed to the Fe^{III} precipitate at pH 7.0 and that surface-catalysed Fe^{II} oxidation accounts for >99 % of the total Fe^{II} oxidation (calculation based on conditional sorption coefficient for Fe^{II} on ferrihydrite in 10 mM bicarbonate electrolyte at pH 7.0[42] assuming sorption equilibrium and based on oxidation rates for dissolved Fe^{II}[36] and adsorbed Fe^{II} on ferrihydrite[42] in the same electrolyte, data from Tamura et al.[42] for ferrihydrite formed by forced hydrolysis of dissolved Fe^{III}). The corresponding conditional rate coefficient of 0.6 min^{-1} for the oxidation of adsorbed Fe^{II} in aerated solution ($pO_2 = 0.2$ atm) corresponds to a half-life time of ~1.2 min, i.e. more than 10 times lower than the half-life time of ~15 min estimated for autocatalytic oxidation of 15 mg L^{-1} Fe^{II} in aerated solution. These calculations indicate that Fe^{II} oxidation in the studied sand filter is dominantly due to surface-catalysed oxidation on accumulated Fe^{III} coatings, in line with model calculations reported in a recent review on Fe removal mechanisms in rapid sand filtration.[9] However, some contribution of microbial Fe^{II} oxidation cannot be ruled out, which may be fostered by microaerophilic conditions in parts of the filter pore space with limited water flow.[9]

The oxidation of dissolved Fe^{II} by O_2 mediates the (at least partial) co-oxidation of dissolved As^{III} to As^{V} by reaction intermediates,[14] and adsorbed As^{III} on ferrihydrite is rapidly co-oxidised during oxidation of Fe^{II} by O_2.[43] Although data on the respective reaction rates is limited, both homogeneous and surface-catalysed Fe^{II} oxidation by O_2 may drive rapid co-oxidation of dissolved or adsorbed As^{III} during water filtration. Furthermore, oxidation of As^{III} could also be induced by Fe^{II} adsorption to Fe^{III}-(oxyhydr)oxide coatings even under anoxic conditions.[44] Upon filter drainage and aeration, residual adsorbed As^{III} may undergo further slow oxidation by O_2,[45] in line with the dominance of As^{V} in the studied filter samples.

Processes involved in Mn retention and role of accumulated $Mn^{IV/III}$ oxide

In contrast to Fe, P and As which became accumulated as fine coatings throughout the sand matrix, Mn became accumulated as pure $Mn^{IV/III}$-(oxyhydr)oxide in separate concretions and coatings (Figs 3, 4, 6). The average amount of 16.8 mmol kg^{-1} accumulated $Mn^{IV/III}$-oxide (Table 2) corresponds to 71 mmol L^{-1} of pore volume. Even based on the unrealistic assumption that this $Mn^{IV/III}$-oxide is entirely available for abiotic surface-catalysed Mn^{II} oxidation in air-saturated water at pH 7.0 and that all Mn^{II} in the passing groundwater readily (and exclusively) adsorbs to these $Mn^{IV/III}$-oxides, a pseudo-first-order rate coefficient of ~0.9 day^{-1} can be estimated from kinetic rates,[18] indicating that

abiotic surface-catalysed Mn^{II} oxidation on $Mn^{IV/III}$-oxides cannot explain effective Mn removal during filtration. Mediated Mn^{II} oxidation by reactive intermediates of Fe^{II} oxidation (in analogy to mediated As^{III} co-oxidation[14]) is not expected to occur because Mn^{III} and Mn^{IV} are strong oxidants that undergo rapid reduction by reaction with Fe^{II}.[18,46] Most probably, the formation of localised Mn-rich coatings is thus due to catalysed coupled biotic–abiotic Mn^{II} oxidation involving Mn-oxidising bacteria and surface-catalysed Mn^{II} oxidation on fresh $Mn^{III/IV}$-oxides.[20,21,47] In addition, Mn^{II} uptake by Mn^{IV}-(oxyhydr)oxides by a comproportionation mechanism[48] could contribute to Mn removal. Considering that μ-XRF analyses suggested that minor fractions of Mn were associated with Fe coatings (~0.01 Mn/Fe), Fe coatings might contribute to Mn retention by acting as a temporary adsorbent for Mn^{II} during a filtration event with subsequent Mn^{II} oxidation on Mn-rich coatings.

$Mn^{IV/III}$ oxides are effective oxidants for both Fe^{II}[22,49,50] and As^{III}.[23,51,52] Even though only a small fraction of the 71 mmol $Mn^{IV/III}$-(oxyhydr)oxide accumulated per litre of pore volume may be accessible to passing groundwater, comparison with the 0.29 mM Fe in the influent groundwater clearly indicates that the Mn-rich coatings and Mn concretions carry a high Fe^{II} and As^{III} oxidation capacity. Indeed, element distribution maps collected on Mn-rich coatings showed that they also contained thin Fe layers (Fig. 4), indicating that Fe^{II} (and probably also As^{III}) oxidation by $Mn^{IV/III}$-(oxyhydr)oxide periodically occurred. However, the distribution patterns of Fe and As in relation to Mn in the three areas mapped by μ-XRF (Figs 3, S3, S4) suggest that this mode of Fe (and As) oxidation and retention was of minor importance compared to surface-catalysed Fe^{II} oxidation on Fe coatings and mediated As^{III} co-oxidation. Nevertheless, $Mn^{IV/III}$-(oxyhydr)oxides may play an important role by buffering and preventing As and Fe mobilisation and release if the filter is temporarily operated without sufficient aeration or if elevated inputs of organic carbon induce higher microbial respiration rates. Depending on the extent to which reductively formed Mn^{II} can be retained by sorption (e.g. cation exchange on clay minerals or adsorption to Fe^{III}-(hydr)oxide coatings) or precipitation reactions (e.g. with calcite), such periodic events, however, might lead to elevated Mn^{II} concentrations in the filter effluent.

Precipitate accumulation in the filter pore space

The studied filter still performed well after 8 years of operation without sand replacement (except for annual replacement of the surface sand layer), indicating that filter clogging did not occur. From the average accumulated amount of Fe in the filter sand of 405 mmol kg^{-1} and based on an ideal ferrihydrite stoichiometry ($FeO_{1.4}(OH)_{0.2}$; 81.7 g mol^{-1}[41]), a dry Fe-precipitate mass of ~33 g kg^{-1} filter sand is calculated. Assuming a density of ~4 g cm^{-3} (for ~6-nm diameter ferrihydrite crystallites[41]), this corresponds to ~3.5 % of the total pore volume (considering bulk density of 1.47 kg L^{-1} and porosity of 35 %). This clearly indicates that even after use for 8 years the filter still retained a substantial capacity for further precipitate formation and P and As retention. The formation of relatively dense precipitate coatings on sand grains may be attributed to the periodic drying of the filter sand, which causes gel-like hydrated ferrihydrite to aggregate into dense particles that will not fully disperse again upon rehydration,[53] resulting in reduced precipitate volume.

Due to the high Ca concentration of ~4 mM in the influent (Table 1), precipitation of calcite in the pore space could also have affected filter performance. XRD results (Fig. S1) indeed confirmed the presence of calcite in the sand material, and the cemented Ca-rich sand crust on the left side of the filter surface (Fig. 1) was attributed to calcite precipitation. Comparison of the influent and effluent Ca concentrations (Table 1), however, indicated that only a small fraction (~6 ± 2 %) of the dissolved Ca was retained in the filter. Most probably, calcite precipitation was limited by the extent of CO_2 out-gassing and occurred mainly at the sand surface. Therefore, and because the top 2–3 cm of filter sand were annually replaced, calcite precipitation did not adversely affect filter performance.

Conclusions and implications

In the investigated household sand filter, effective removal and retention of Fe, As and P can be attributed to several factors: (i) The raw groundwater water is characterised by relatively high Fe/As and Fe/P ratios that would also result in effective P and As co-precipitation during water aeration even in the absence of sand surfaces and microorganisms. (ii) The anoxic groundwater is effectively aerated in the studied sand filter. (iii) High concentrations of Ca and Mg in the groundwater prevent the formation of mobile As-containing Fe^{III} colloids. (iv) The high amounts of accumulated ferrihydrite-like Fe coatings ensure rapid adsorption of Fe^{II}, P and As, and surface-catalysed oxidation of Fe^{II} and co-oxidation of As^{III}. (v) Filter drainage and partial drying after use promote the complete oxidation of residual Fe^{II} and As^{III} and the formation of more compact Fe-coatings that limit the risk of filter clogging. (vi) Inhibited crystallisation of the Fe^{III} precipitates over time by adsorbed Si prevents the remobilisation of accumulated As and P. Based on theoretical calculations, autocatalytic and surface-catalysed Fe^{II} oxidation on ferrihydrite-like sand coatings dominate Fe^{II} oxidation, whereas microbial Fe oxidation is likely of minor importance for effective removal of Fe, As and P. Mn is accumulated in separate Mn-rich coatings and concretions and the slow kinetics of purely abiotic surface-catalysed oxidation suggest that Mn^{II}-oxidising bacteria play a key role in Mn removal.

The effectiveness of sand filters for As removal critically depends on the molar P/Fe ratio of the groundwater to be treated.[1] In the case studied here, the groundwater had a P/Fe ratio of 0.063 (Table 1). Considering an adsorption maximum of ~0.25 oxyanion/Fe for a ferrihydrite-like precipitate,[11,12] this study thus shows that effective As removal can be achieved at a groundwater P/Fe ratio of up to one fourth the sorption capacity of ferrihydrite-type precipitates, and that both P and As are not released back into solution over time because Si inhibits precipitate aging. At higher P/Fe ratios of the groundwater, however, saturation of the Fe^{III} precipitate and precipitate aging are expected to reduce filter performance. In these cases, effective As removal requires additional Fe, for example from electrocoagulation before filtration[54,55] or from zerovalent iron implemented in the filter matrix.[56,57] Where Mn removal is required as well, however, Fe addition should be kept as low as possible to avoid a reduction in Mn removal efficiency.

With respect to the use of household sand filters for As removal from groundwater, it has been recommended that the sand should be replaced in regular intervals (i.e. every 3–6 months).[7] Considering the beneficial role of accumulated Fe and Mn coatings and the probable importance of microbial Mn oxidation, it appears that filter sand may be used over longer periods of time depending on the chemistry of the raw

groundwater. As discussed previously,[1,7] safe disposal of the spent sand is required to prevent re-introduction of As into soil or groundwater. Mixing a fraction of previously used filter sand with fresh sand, however, may aid to rapidly establish effective filter performance after sand exchange by introducing reactive surface coatings and active Mn^{II}-oxidising microbial populations.

Supplementary material

The Supplementary material is available from the journal online (see http://www.publish.csiro.au/?act=view_file&file_id=EN14011_ AC.pdf).

Acknowledgements

The Angströmquelle Karlsruhe (ANKA, Eggenstein-Leopoldshafen, Germany) and the Swiss Norwegian Beamline (SNBL) at the European Synchrotron Radiation Facility (ESRF, Grenoble, France) are acknowledged for the provision of XAS beamtime. The authors thank Herman Emerich and Wouter van Beek (SNBL, ESRF) for their assistance with data collection at the SNBL. Sam Webb (Stanford Synchrotron Radiation Laboratory, Menlo Park, CA, USA) is acknowledged for providing Mn K-edge XAS reference spectra of δ-MnO_2 and todorokite. Caroline Stengel, Numa Pfenninger, Irene Brunner and Sandro Fazzolari (Eawag, Dübendorf, Switzerland) are acknowledged for their help with field and laboratory work and Anna-Caterina Senn (Eawag) for help with XAS data collection. AK and KN acknowledge funding from the German research foundation (DFG; KA 1736/22–1).

References

[1] S. J. Hug, O. X. Leupin, M. Berg, Bangladesh and Vietnam: different groundwater compositions require different approaches to arsenic mitigation. *Environ. Sci. Technol.* **2008**, *42*, 6318. doi:10.1021/ES7028284

[2] M. F. Ahmed, S. Ahuia, M. Alauddin, S. J. Hug, J. R. Lloyd, A. Pfaff, T. Pichler, C. Saltikov, M. Stute, A. van Geen, Epidemiology – ensuring safe drinking water in Bangladesh. *Science* **2006**, *314*, 1687. doi:10.1126/SCIENCE.1133146

[3] M. Berg, H. C. Tran, T. C. Nguyen, H. V. Pham, R. Schertenleib, W. Giger, Arsenic contamination of groundwater and drinking water in Vietnam: a human health threat. *Environ. Sci. Technol.* **2001**, *35*, 2621. doi:10.1021/ES010027Y

[4] P. L. Smedley, D. G. Kinniburgh, A review of the source, behaviour and distribution of arsenic in natural waters. *Appl. Geochem.* **2002**, *17*, 517. doi:10.1016/S0883-2927(02)00018-5

[5] A. Horneman, A. Van Geen, D. V. Kent, P. E. Mathe, Y. Zheng, R. K. Dhar, S. O'Connell, M. A. Hoque, Z. Aziz, M. Shamsudduha, A. A. Seddique, K. M. Ahmed, Decoupling of As and Fe release from Bangladesh groundwater under reducing conditions. Part I. Evidence from sediment profiles. *Geochim. Cosmochim. Acta* **2004**, *68*, 3459. doi:10.1016/J.GCA.2004.01.026

[6] F. S. Islam, A. G. Gault, C. Boothman, D. A. Polya, J. M. Charnock, D. Chatterjee, J. R. Lloyd, Role of metal-reducing bacteria in arsenic release from Bengal delta sediments. *Nature* **2004**, *430*, 68. doi:10.1038/NATURE02638

[7] M. Berg, S. Luzi, P. T. K. Trang, P. H. Viet, W. Giger, Arsenic removal from groundwater by household sand filters: comparative field study, model calculations, and health benefits. *Environ. Sci. Technol.* **2006**, *40*, 5567. doi:10.1021/ES060144Z

[8] R. Tobias, M. Berg, Sustainable use of arsenic-removing sand filters in Vietnam: psychological and social factors. *Environ. Sci. Technol.* **2011**, *45*, 3260. doi:10.1021/ES102076X

[9] C. G. E. M. van Beek, T. Hiemstra, B. Hofs, M. M. Nederlof, J. A. M. van Paassen, G. K. Reijnen, Homogeneous, heterogeneous and biological oxidation of iron(II) in rapid sand filtration. *J. Water Supply* **2012**, *61*, 1.

[10] R. Kaegi, A. Voegelin, D. Folini, S. J. Hug, Effect of phosphate, silicate, and Ca on the morphology, structure and elemental composition of Fe(III)-precipitates formed in aerated Fe(II) and As(III) containing water. *Geochim. Cosmochim. Acta* **2010**, *74*, 5798. doi:10.1016/J.GCA.2010.07.017

[11] A. Voegelin, R. Kaegi, J. Frommer, D. Vantelon, S. J. Hug, Effect of phosphate, silicate, and Ca on Fe(III)-precipitates formed in aerated Fe(II)- and As(III)-containing water studied by X-ray absorption spectroscopy. *Geochim. Cosmochim. Acta* **2010**, *74*, 164. doi:10.1016/J.GCA.2009.09.020

[12] A. Voegelin, A.-C. Senn, R. Kaegi, S. J. Hug, S. Mangold, Dynamic Fe-precipitate formation induced by Fe(II) oxidation in aerated phosphate-containing water. *Geochim. Cosmochim. Acta* **2013**, *117*, 216. doi:10.1016/J.GCA.2013.04.022

[13] J. Miot, K. Benzerara, G. Morin, A. Kappler, S. Bernard, M. Obst, C. Férard, F. Skouri-Panet, J.-M. Guigner, N. Posth, M. Galvez, G. E. Brown, F. Guyot, Iron biomineralization by anaerobic neutrophilic iron-oxidizing bacteria. *Geochim. Cosmochim. Acta* **2009**, *73*, 696. doi:10.1016/J.GCA.2008.10.033

[14] S. J. Hug, O. Leupin, Iron-catalyzed oxidation of arsenic(III) by oxygen and by hydrogen peroxide: pH-dependent formation of oxidants in the Fenton reaction. *Environ. Sci. Technol.* **2003**, *37*, 2734. doi:10.1021/ES026208X

[15] R. S. Oremland, J. F. Stolz, The ecology of arsenic. *Science* **2003**, *300*, 939. doi:10.1126/SCIENCE.1081903

[16] L. C. Roberts, S. J. Hug, T. Ruettimann, M. M. Billah, A. W. Khan, M. T. Rahman, Arsenic removal with iron(II) and iron(III) in waters with high silicate and phosphate concentrations. *Environ. Sci. Technol.* **2004**, *38*, 307. doi:10.1021/ES0343205

[17] X. G. Meng, G. P. Korfiatis, S. B. Bang, K. W. Bang, Combined effects of anions on arsenic removal by iron hydroxides. *Toxicol. Lett.* **2002**, *133*, 103. doi:10.1016/S0378-4274(02)00080-2

[18] J. J. Morgan, in *Metal Ions in Biological Systems* (Eds A. Sigel, H. Sigel) **2000**, pp. 1–34 (Marcel Dekker Inc.: New York).

[19] B. M. Tebo, J. R. Bargar, B. G. Clement, G. J. Dick, K. J. Murray, D. Parker, R. Verity, S. M. Webb, Biogenic manganese oxides: properties and mechanisms of formation. *Annu. Rev. Earth Planet. Sci.* **2004**, *32*, 287. doi:10.1146/ANNUREV.EARTH.32.101802.120213

[20] D. R. Learman, S. D. Wankel, S. M. Webb, N. Martinez, A. S. Madden, C. M. Hansel, Coupled biotic-abiotic Mn(II) oxidation pathway mediates the formation and structural evolution of biogenic Mn oxides. *Geochim. Cosmochim. Acta* **2011**, *75*, 6048. doi:10.1016/J.GCA.2011.07.026

[21] F. Luan, C. M. Santelli, C. M. Hansel, W. D. Burgos, Defining manganese(II) removal processes in passive coal mine drainage treatment systems through laboratory incubation experiments. *Appl. Geochem.* **2012**, *27*, 1567. doi:10.1016/J.APGEOCHEM.2012.03.010

[22] D. Postma, Concentration of Mn and separation from Fe in sediments – I. Kinetics and stoichiometry of the reaction between birnessite and dissolved Fe(II) at 10 °C. *Geochim. Cosmochim. Acta* **1985**, *49*, 1023. doi:10.1016/0016-7037(85)90316-3

[23] S. C. Ying, B. D. Kocar, S. Fendorf, Oxidation and competitive retention of arsenic between iron- and manganese oxides. *Geochim. Cosmochim. Acta* **2012**, *96*, 294. doi:10.1016/J.GCA.2012.07.013

[24] Y. T. He, J. G. Hering, Enhancement of arsenic(III) sequestration by manganese oxides in the presence of iron(II). *Water Air Soil Pollut.* **2009**, *203*, 359. doi:10.1007/S11270-009-0018-8

[25] B. Ravel, M. Newville, ATHENA, ARTEMIS, HEPHAESTUS: data analysis for X-ray absorption spectroscopy using IFEFFIT. *J. Synchrotron Radiat.* **2005**, *12*, 537. doi:10.1107/S0909049505012719

[26] S. Preibisch, S. Saalfeld, P. Tomancak, Globally optimal stitching of microscopic image acquisiations. *Bioinformatics* **2009**, *25*, 1463. doi:10.1093/BIOINFORMATICS/BTP184

[27] J. Schindelin, I. Arganda-Carreras, E. Frise, V. Kaynig, M. Longair, T. Pietzsch, S. Preibisch, C. Rueden, S. Saalfeld, B. Schmid, J.-Y. Tinevez, D. J. White, V. Hartenstein, K. Eliceiri, P. Tomancak,

A. Cardona, Fiji: an open-source platform for biological-image analysis. *Nat. Methods* **2012**, *9*, 676. doi:10.1038/NMETH.2019

[28] M. Berg, C. Stengel, P. T. K. Trang, P. H. Viet, M. L. Sampson, M. Leng, S. Samreth, D. Fredericks, Magnitude of arsenic pollution in the Mekong and Red River deltas – Cambodia and Vietnam. *Sci. Total Environ.* **2007**, *372*, 413. doi:10.1016/J.SCITOTENV.2006.09.010

[29] A. Kappler, K. S. Nitzsche, A. Bhansali, M. Berg, P. T. K. Trang, P. H. Viet, S. Behrens, Microbial Fe, Mn & As redox transformations and their contributions to As removal from drinking water in household sand filters in Vietnam. *Mineral. Mag.* **2012**, *76*, 1918.

[30] J. Rose, A. Manceau, J. Y. Bottero, A. Masion, F. Garcia, Nucleation and growth mechanisms of Fe oxyhydroxide in the presence of PO_4 ions. 1. Fe K-edge EXAFS study. *Langmuir* **1996**, *12*, 6701. doi:10.1021/LA9606299

[31] G. S. Pokrovski, J. Schott, F. Farges, J.-L. Hazeman, Iron(III)–silicate interactions in aqueous solution: insights from X-ray absorption fine structure spectroscopy. *Geochim. Cosmochim. Acta* **2003**, *67*, 3559. doi:10.1016/S0016-7037(03)00160-1

[32] J. A. Wilkie, J. G. Hering, Adsorption of arsenic onto hydrous ferric oxide: effects of adsorbate/adsorbent ratios and co-occurring solutes. *Colloids Surf. A* **1996**, *107*, 97. doi:10.1016/0927-7757(95)03368-8

[33] C. M. van Genuchten, J. Peña, S. E. Amrose, A. J. Gadgil, Structure of Fe(III) precipitates generated by the electrolytic dissolution of Fe(0) in the presence of groundwater ions. *Geochim. Cosmochim. Acta* **2014**, *127*, 285. doi:10.1016/J.GCA.2013.11.044

[34] A. Gunnars, S. Blomqvist, P. Johansson, C. Andersson, Formation of Fe(III) oxyhydroxide colloids in freshwater and brackish seawater, with incorporation of phosphate and calcium. *Geochim. Cosmochim. Acta* **2002**, *66*, 745. doi:10.1016/S0016-7037(01)00818-3

[35] U. Tessenow, Lösungs-, Diffusions- und Sorptionsprozesse in der Oberschicht von Seesedimenten. IV. Reaktionsmechanismen und Gleichgewichte im System Eisen-Mangan-Phosphat im Hinblick auf die Vivianitakkumulation im Ursee. *Arch. Hydrobiol.* **1974**, *47*(Suppl.), 1.

[36] H. Tamura, K. Goto, M. Nagayama, The effect of ferric hydroxide on the oxygenation of ferrous ions in neutral solutions. *Corros. Sci.* **1976**, *16*, 197. doi:10.1016/0010-938X(76)90046-9

[37] S. Jessen, F. Larsen, C. Bender Koch, E. Arvin, Sorption and desorption of arsenic to ferrihydrite in a sand filter. *Environ. Sci. Technol.* **2005**, *39*, 8045. doi:10.1021/ES050692X

[38] L. Carlson, U. Schwertmann, Iron and manganese oxides in Finnish ground water treatment plants. *Water Res.* **1987**, *21*, 165. doi:10.1016/0043-1354(87)90045-5

[39] R. K. Vempati, R. H. Loeppert, Influence of structural and adsorbed Si on the transformation of synthetic ferrihydrite. *Clays Clay Miner.* **1989**, *37*, 273. doi:10.1346/CCMN.1989.0370312

[40] D. T. Mayer, W. M. Jarrell, Phosphorus sorption during iron(II) oxidation in the presence of dissolved silica. *Water Res.* **2000**, *34*, 3949. doi:10.1016/S0043-1354(00)00158-5

[41] T. Hiemstra, Surface and mineral structure of ferrihydrite. *Geochim. Cosmochim. Acta* **2013**, *105*, 316. doi:10.1016/J.GCA.2012.12.002

[42] H. Tamura, S. Kawamura, M. Hagayama, Acceleration of the oxidation of Fe^{2+} ions by Fe(III)-oxyhydroxides. *Corros. Sci.* **1980**, *20*, 963. doi:10.1016/0010-938X(80)90077-3

[43] G. Ona-Nguema, G. Morin, Y. Wang, A. L. Foster, F. Juillot, G. Calas, G. E. Brown, XANES evidence for rapid arsenic(III) oxidation at magnetite and ferrihydrite surfaces by dissolved O_2 via Fe^{2+}-mediated reactions. *Environ. Sci. Technol.* **2010**, *44*, 5416. doi:10.1021/ES1000616

[44] K. Amstaetter, T. Borch, P. Larese-Casanova, A. Kappler, Redox transformation of arsenic by Fe^{II}-activated goethite (α-FeOOH). *Environ. Sci. Technol.* **2010**, *44*, 102. doi:10.1021/ES901274S

[45] Z. Zhao, Y. Jia, L. Xu, S. Zhao, Adsorption and heterogeneous oxidation of As(III) on ferrihydrite. *Water Res.* **2011**, *45*, 6496. doi:10.1016/J.WATRES.2011.09.051

[46] J. E. Kostka, G. W. Luther III, K. H. Nealson, Chemical and biological reduction of Mn(III)-pyrophosphate complexes: potential importance of dissolved Mn(III) as an environmental oxidant. *Geochim. Cosmochim. Acta* **1995**, *59*, 885.

[47] J. Vandenabeele, D. de Beer, R. Germonpré, W. Verstraete, Manganese oxidation by microbial consortia from sand filters. *Microb. Ecol.* **1992**, *24*, 91. doi:10.1007/BF00171973

[48] E. J. Elzinga, Reductive transformation of birnessite by aqueous Mn(II). *Environ. Sci. Technol.* **2011**, *45*, 6366. doi:10.1021/ES2013038

[49] D. Postma, C. A. J. Appelo, Reduction of Mn-oxides by ferrous iron in a flow system: column experiment and reactive transport modeling. *Geochim. Cosmochim. Acta* **2000**, *64*, 1237. doi:10.1016/S0016-7037(99)00356-7

[50] J. E. Villinski, P. A. O'Day, T. L. Corley, M. H. Conklin, In situ spectroscopic and solution analyses of the reductive dissolution of MnO_2 by Fe(II). *Environ. Sci. Technol.* **2001**, *35*, 1157. doi:10.1021/ES001356D

[51] X. Han, Y.-L. Li, J.-D. Gu, Oxidation of As(III) by MnO_2 in the absence and presence of Fe(II) under acidic conditions. *Geochim. Cosmochim. Acta* **2011**, *75*, 368. doi:10.1016/J.GCA.2010.10.010

[52] C. Tournassat, L. Charlet, D. Bosbach, A. Manceau, Arsenic(III) oxidation by birnessite and precipitation of manganese(II) arsenate. *Environ. Sci. Technol.* **2002**, *36*, 493. doi:10.1021/ES0109500

[53] A. C. Scheinost, S. Abend, K. I. Pandya, D. L. Sparks, Kinetic controls on Cu and Pb sorption by ferrihydrite. *Environ. Sci. Technol.* **2001**, *35*, 1090. doi:10.1021/ES000107M

[54] L. Li, C. M. van Genuchten, S. E. A. Addy, J. Yao, N. Gao, A. J. Gadgil, Modeling As(III) oxidation and removal with iron electrocoagulation in groundwater. *Environ. Sci. Technol.* **2012**, *46*, 12 038. doi:10.1021/ES302456B

[55] C. M. van Genuchten, S. E. A. Addy, J. Pena, A. J. Gadgil, Removing arsenic from synthetic groundwater with iron electrocoagulation: an Fe and As K-edge EXAFS study. *Environ. Sci. Technol.* **2012**, *46*, 986. doi:10.1021/ES201913A

[56] A. Neumann, R. Kaegi, A. Voegelin, A. Hussam, A. K. M. Munir, S. J. Hug, Arsenic removal with composite iron matrix filters in Bangladesh: a field and laboratory study. *Environ. Sci. Technol.* **2013**, *47*, 4544. doi:10.1021/ES305176X

[57] O. X. Leupin, S. J. Hug, A. B. M. Badruzzaman, Arsenic removal from Bangladesh tube well water with filter columns containing zerovalent iron filings and sand. *Environ. Sci. Technol.* **2005**, *39*, 8032. doi:10.1021/ES050205D

[58] J. Frommer, A. Voegelin, J. Dittmar, M. A. Marcus, R. Kretzschmar, Biogeochemical processes and arsenic enrichment around rice roots in paddy soil: results from micro-focused X-ray spectroscopy. *Eur. J. Soil Sci.* **2011**, *62*, 305. doi:10.1111/J.1365-2389.2010.01328.X

[59] S. M. Webb, B. M. Tebo, J. R. Bargar, Structural characterization of biogenic Mn oxides produced in seawater by the marine *Bacillus* sp. strain SG-1. *Am. Min.* **2005**, *90*, 1342. doi:10.2138/AM.2005.1669